

# Modelling Ultra High Pressure Compaction of Powder

P. Jonsén, H.-Å. Häggblad, S. Berg

*The use of high pressure high temperature (HPHT) equipment varies; in mineral physics research the equipment is used for investigation of the earth's interior and in industry it is used for commercially produced synthetic diamonds and other polycrystalline products. The common denominator for almost all high pressure systems is to use capsules where a powder material encloses the core material. Numerical analysis of the manufacturing processes with working conditions which reaches ultra high pressure (above 10 GPa) requires a constitutive model which can handle the specific behaviours of the powder from a low density to solid state. Calcium carbonate ( $\text{CaCO}_3$ ) is a mineral that can be used in high pressure processes and is very common in the earth core. A constitutive model for calcium carbonate applied to high pressure compaction is presented. The plastic response of powder is non-linear and described in a rate-independent cap plasticity model. The cap model has been developed to capture the behaviour of minerals in high pressure applications. The yield function consists of a failure envelope fitted to a strain-hardening cap. Experimental tests with a Bridgman anvil set-up using calcium carbonate powder discs are performed. Numerical analysis using the finite element method is done to virtually reproduce the experiments. Results from the analysis are compared to measured experimental results. The numerical analyses agree reasonably well with the experimental results.*

## 1 Introduction

High pressure sintering is a means to improve the material properties, either through new sintering aids becoming available at higher pressures or through improving intergranular bonding. Synthetic diamonds have usually been sintered using cobalt metal as sintering aid. However, the metal agent causes deterioration such as graphitization at high temperatures. To overcome this issue and obtain a thermally stable polycrystalline diamond other agents have been studied. Commonly used agents are metal carbonates such as  $\text{CaCO}_3$ ,  $\text{MgCO}_3$  and  $\text{SrCO}_3$ . Ueda et al. (1996) and Akaishi et al. (1996) sintered diamond using  $\text{MgCO}_3$  at a pressure of 7.7 GPa and temperature of 2000° C. Others have also sintered diamond using  $\text{CaCO}_3$  (Westraadt et al., 2007) and oxide or double oxide compounds of iron family elements, such as  $\text{FeTiO}_3$ ,  $\text{Fe}_2\text{SiO}_4$  and  $\text{Y}_3\text{Fe}_5\text{O}$  (Sumiya and Satoh, 1999). In addition, the technology of sintering various types of nano-powder into compacts has grown steadily in recent years. The nano-powder requires a high sintering pressure, up to 8 GPa (Lu et al., 2006; Gallas et al., 1997; Li et al., 2000). These materials are being increasingly commercialized, and the modelling of different geometries and mixtures as well as the exploration of the material properties up to very high pressures will therefore become more important in the near future.

Several systems have been developed to sustain pressure of 10 GPa (Fukunaga et al., 1999; Kanke et al., 2002; Taniguchi et al., 2004) or more. The development of these systems are mainly based on experience and trial and error. A numerical analysis can be of assistance in design, development and optimisation of these systems. The analyses require some critical features and aspects of nonlinear analysis. The pressing process is highly nonlinear due to the material response, contact boundary conditions, and friction behaviour. Because of the difficulty obtaining the data required, numerical analysis of high-pressure powder compaction are scarce. Several procedures have been developed to exploit experimental results in determining parameters for constitutive models (Han et al., 2008; Brinckmann et al., 2009; Berg et al., 2010). Constitutive parameters can be obtained using experimental techniques like diametrical compression tests, uniaxial tests and closed die tests. In Li et al. (2007) the cubic anvil pressing (Sung, 1997) of pyrophyllite is numerically analysed using a Drucker-Prager model. In Berg et al. (2011, 2012c) a cap plasticity model is used to analyse the compaction of calcite in the Bridgman anvil high-pressure apparatus (Graham, 1986, Wakatsuki et al., 1972).

One important part of a constitutive model is the elastic relation. It has been shown that the elastic behaviour of the powder compact changes with density, see Berg et al. (2010). A non-destructive method that generates elastic data is ultrasonic pulse-echo measurements. It is a method for determining the elastic properties of materials

using two different ultrasonic velocities, a longitudinally wave velocity and a shear wave velocity. This method has been used by several authors to investigate the elastic properties of different materials. For example, Carlson et al. (2003) investigated CaSO<sub>4</sub>-based bone cement and determined the adiabatic bulk modulus and densities as the mould settled. Fukuhara et al. (2007) investigated porous glassy alloys in terms of porosity versus elastic parameters.

The purpose of the study in this paper is to develop a constitutive model for ultra high pressure compaction of powder. Here is ultra high pressure defined as mean stress of 10<sup>10</sup> Pa in compression. Both low and very high pressures are addressed. The model should be able to numerically reproduce the pressing process of powder from low density to full density, with both elastic and plastic properties correctly related to the whole span of density and load state. The present understanding of constitutive modelling is either restricted in density or developed for solid materials, not the complete range of density and stress state. This is why it is a need for better understanding and increased knowledge in this field.

## 2 Material

The powder used in this investigation is spray dried CaCO<sub>3</sub> also called calcite, which is the main part of limestone. To ease the pressing process, a small amount of wax and poly vinyl alcohol (PVA) was added to the powder as lubricants. The moisture level of the powder, when pressed, was 0.7%. ±0.025%. The moisture level together with the lubricants gives a full density around 2600 kg/m<sup>3</sup>. The full density of a single crystal calcite is 2710 kg/m<sup>3</sup>. A scanning electron microscopy (SEM) analysis of the powder shows that some large granules are formed, mostly due to clustering of smaller granules, see Figure 1.

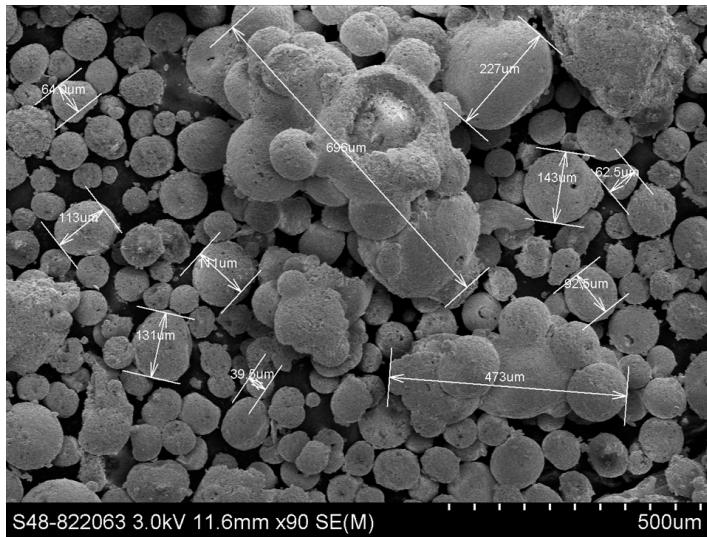


Figure 1. SEM picture including size measurements of spray dried granules. Large particles have formed due to clustering

## 3 Constitutive Model

The constitutive model is divided into elastic and elastic-plastic parts.

### 3.1 Elasticity Model

The elastic properties change as a function of density

$$\sigma = D^{el}(\rho_r)\varepsilon^{el} \quad (1)$$

where  $\sigma$  is the stress tensor,  $D^{el}$  is the elastic stiffness matrix,  $\varepsilon^{el}$  is the elastic strain tensor and  $\rho_r$  is the relative density. The relative density is divided into elastic and plastic parts such that the plastic relative density is the remaining density after unloading defined as

$$\rho_r^p = \rho_r - \rho_r^e \quad (2)$$

The elastic properties of calcite powder were investigated by Berg et al. (2010). It was found that the Young's modulus increased with increasing density. In Berg et al. (2012b) an investigation of density-dependent Poisson's ratio was made using ultrasonic measurements. The data was fitted to a polynomial function for the Poisson's ratio

$$\nu = -12.069(\rho_r^p)^3 + 31.699(\rho_r^p)^2 - 26.484\rho_r^p + 7.1697 \quad (3)$$

To complete the elastic model a density dependent bulk modulus is used. The bulk modulus is divided into two parts, one which only depends on the plastic part of the relative density and one which also depends on the elastic part of the relative density. This is done to handle the bulk modulus increase due to stress, which exists for full dense powder.

$$K = K_e K_p \quad (4)$$

For the part depending in the plastic relative density (or the plastic volumetric strain) the following function is used:

$$K_p = K_s \left( \frac{P_1}{P_2} \right)^{\frac{(\rho_c(\exp(\text{abs}(\varepsilon_v^p)))-1)}{(1-\rho_c)}} \quad (5)$$

where  $K_s$  is the solid bulk modulus,  $P_1$  and  $P_2$  are parameters that will be optimized to experimental data,  $\varepsilon_v^p$  is the plastic volumetric strain, and  $\rho_c$  the initial relative density. To account for the influence of the elastic relative density on the bulk modulus, an Equation of State (EoS) by Knittle, (1995) is added.

$$K_e = \frac{\rho_r^e + \rho_r^p}{\rho_r^p} \left[ \ln\left(\frac{\rho_r^e + \rho_r^p}{\rho_r^p}\right) + 1 \right] \quad (6)$$

This gives the complete expression for the bulk modulus.

$$K = \frac{\rho_r^e + \rho_r^p}{\rho_r^p} \left[ \ln\left(\frac{\rho_r^e + \rho_r^p}{\rho_r^p}\right) + 1 \right] K_s \left( \frac{P_1}{P_2} \right)^{\frac{(\rho_c(\exp(\text{abs}(\varepsilon_v^p)))-1)}{(1-\rho_c)}} \quad (7)$$

### 3.2. Plasticity Model

For a generalized plasticity theory we need:

- A yield function (criterion) specified by a scalar function describing the transition from an elastic state to an elastic-plastic state.
- A flow rule.
- A hardening rule which describes the evolution of the yield surface.

#### *Cap model yield surfaces*

A basic assumption when developing a mathematical theory of plasticity is that there exist a continuous yield function  $f(x)$  with the properties as follows:

- The function  $f$  represents a closed surface, i.e. yield function, in the stress space.
- The plastic strain rate vanish in the region  $f < 0$ . Called the elastic region.
- The plastic strain rate can be non-zero in the region  $f = 0$ .

For a work hardening material the yield function can be stated as

$$f(\sigma_{ij}, \kappa) = 0 \quad (8)$$

where  $\kappa$  is an internal state hardening parameter normally taken as a function of the plastic volumetric strain. For an isotropic material the yield function can be taken as

$$f(I_1, \sqrt{J_2}, \kappa) = 0 \quad (9)$$

where  $I_1$  is the first stress invariant and  $J_2$  is the second deviatoric stress invariant. In general the cap model consists of two different yield surfaces, the shear failure surface,  $f_1$ , and the strain-hardening cap,  $f_2$

$$f_1(I_1, \sqrt{J_2}) = \sqrt{J_2} - f(I_1) = 0 \quad (10)$$

$$f_2(I_1, \sqrt{J_2}, \kappa) = \sqrt{J_2} - f(I_1, \kappa) = 0 \quad (11)$$

#### *Powder compaction cap model*

One essential feature of the cap model for powder compaction is that it is able to yield under pressure. There are different types of cap models where the shear-failure surface function is written in slightly different forms, for example Drucker-Prager cap and DiMaggio-Sandler cap model (Sandler et al., 1976; Sandler and Rubin, 1979; Sandler and Baron, 1979; Häggblad, 1991).

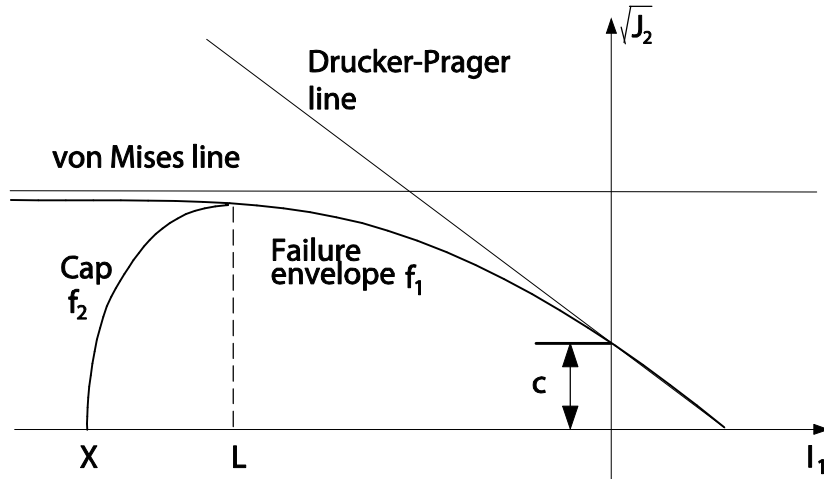


Figure 2. Cap model,  $f_1$  is the failure envelope,  $f_2$  is the moving strain hardening cap and  $C$  is the shear cohesion

The cap model yield surfaces can be seen in Figure 2. The shear failure envelope ( $f_1$ ) of the cap model is modifiable so that it can combine the yield surfaces of Drucker-Prager and von Mises, respectively. At low mean normal compressive stress the Drucker-Prager surface is approached, and at high mean normal stress a von Mises surface is approached.

The original yield surfaces of DiMaggio-Sandler can be written as

$$f_1(I_1, J_2) = \sqrt{J_2} - [\alpha - \gamma \exp(\beta I_1) - \theta I_1] = 0 \quad (12)$$

$$f_2(I_1, J_2, \kappa) = \sqrt{J_2} - \frac{1}{R} \sqrt{(X-L)^2 - (I_1-L)^2} = 0 \quad (13)$$

where  $\alpha$ ,  $\beta$ ,  $\gamma$  and  $\theta$  are material parameters,  $L$  is the point of intersection between the two yield surfaces and  $X$  the point of intersection between the hydrostatic axis and the cap function. The shear cohesion,  $C$ , is the critical shear stress of the material at zero mean stress. The eccentricity parameter  $R$  is the ratio of the horizontal to vertical ellipse axes. It defines the shape of the cap in the plane of the stress tensor first invariant versus the

square root of the second deviatoric invariant. For the inelastic part of the deformation a particular form of yield surface, with associated flow and a hardening rule, is used. It allows the yield surface to grow or shrink.

Since the movement of the shear failure envelope during compaction is non-linear and dependent on density, a movable shear yield surface is introduced. The expressions for the relative density-dependent yield functions presented here are

$$f_1(I_1, J_2) = \sqrt{J_2} - [\alpha - A(\rho_r^p)\gamma \exp(\beta I_1) - \theta I_1] = 0 \quad (14)$$

$$A(\rho_r^p) = \left( a_1 - \exp\left( a_2(\rho_r^p)^{a_3} \right) \right) \quad (15)$$

$$f_2(I_1, J_2, \kappa) = \sqrt{J_2} - \frac{1}{R} \sqrt{(X-L)^2 - (I_1-L)^2} = 0 \quad (16)$$

$A$  controls the movement of the yield surface ( $f_1$ ) and  $a_1$ ,  $a_2$  and  $a_3$  are material parameters, see also Jonsén and Häggblad (2005). The optimized values of the yield surface parameters are as follows:  $\alpha=1144$  MPa,  $\beta=6.928E-10$  (MPa)<sup>-1</sup>,  $\gamma=374$  MPa,  $\theta=0.43$ ,  $a_1=4.06$ ,  $a_2=0.086$  and  $a_3=8.2$ . The eccentricity parameter  $R$  represents the degree of influence of the hydrostatic stress component on the onset of yielding of the porous body and may be a function of the relative density. This influence is introduced for metal powder by the following relation for the equivalent stress value (Svoboda et al., 2006)

$$\sigma_{eq}^2(I_1, J_2) = 3\phi_1 J_2 + \phi_2 I_1^2 \quad (17)$$

where  $\phi_1$  and  $\phi_2$  are functions of relative density. The function  $\phi_2$  should fulfil the requirement that it approaches zero when the relative density approaches one. By rewriting the equation to include a moving cap the following relation can be found

$$\sigma_{eq}^2(I_1, J_2) = J_2 + [\lambda(I_1 - L)]^2 \quad (18)$$

where  $\lambda$  now corresponds to the eccentricity parameter  $R$  such that

$$R = \frac{1}{\lambda} \quad (19)$$

By assuming a first order relation of  $R$  with relative plastic density and fulfilling the requirement above, the following relation is proposed

$$R(\rho_r^p) = (r_1 + k\rho_r^p) \frac{1}{1 - \rho_r^p} \quad (20)$$

where  $r_1$  is the minimum  $R$ -value obtainable and  $k$  is a constant.  $\rho_r^p$  is the relative plastic density.

#### Compaction hardening

A material is said to be hardening when the following two conditions holds:

$$d\sigma_{ij}d\varepsilon_{ij} > 0 \quad \text{upon loading} \quad (21)$$

$$\oint d\sigma_{ij}d\varepsilon_{ij}^p \geq 0 \quad \text{completing a cycle} \quad (22)$$

The first postulate states that strain softening may not occur. The second statement means that the yield surface has to be convex, and that the strain increment vector has to be normal to the yield surface.

The hardening function ( $\kappa$ ) is the expression that controls how the cap yield surface moves in stress space. It is chosen so that

$$L = \kappa \quad (23)$$

Here the cap movement is based upon a relation between the plastic volumetric strain and the cap intersection with the hydrostatic axis

$$\varepsilon_v^p = f(X) \quad (24)$$

The hardening function  $\kappa$  is then implicitly defined as a function of plastic volumetric strain by equations (24), (16) and (23). The plastic volumetric strain is given by the differential relation

$$d\varepsilon_v^p = d\varepsilon_v^p \text{ if } d\varepsilon_v^p \leq 0, \text{ or } \kappa < I_1 \text{ and } \kappa < 0 \quad (25a)$$

$$\text{otherwise } d\varepsilon_v^p = 0 \quad (25b)$$

Equation (25) together with equation (23) limits the shrinking of the cap to  $L = 0$ .

#### *Flow rule*

The flow rule is based on dividing the net strain increment into its elastic and plastic components. The plastic strain increment is assumed to be orthogonal to the stress gradient of a plastic potential function. Further more it is assumed that there exists a plastic potential function  $g$ , so that the plastic strain rate can be derived by

$$d\varepsilon^p = d\lambda \frac{\partial g}{\partial \sigma} \quad (26)$$

where  $d\lambda$  is a plastic flow multiplier that can, for example, be a function of equivalent plastic strain. In this paper the associated flow rule approach is used.

#### *Hardening function*

The following function for the plastic volumetric strain is introduced

$$\varepsilon_v^p(X) = c_1(-X)^{-c_2} - \varepsilon_{vmax} \quad (27)$$

where  $c_1$  and  $c_2$  are two parameters that were least square fitted, and  $\varepsilon_{vmax}$  is maximum volumetric strain. Least square method yielded the values  $c_1=1.80$  and  $c_2=0.23$ . The maximum volumetric strain,  $\varepsilon_{vmax}$ , is set to 1.15.

### **3.3 Friction**

A Coulomb friction model with a constant coefficient of friction of  $\mu=0.255$  is used. The value is found by results from Berg et al. (2012a) where the friction of  $\text{CaCO}_3$  powder mix is measured using a universal Micro Tribometer.

## **4 Numerical Application**

All numerical analysis in this work is done using the explicit FE code LS-DYNA V971 R5.1 together with a user defined material subroutine of the constitutive model described earlier, see Appendix A for the description for the explicit time integration in FEM and Appendix B for the stability condition needed to be fulfilled.

High pressure compaction of powder using the Bridgeman anvil apparatus is analysed. The finite element model is axisymmetric and had reduced integration elements with 2261 nodes, see Figure 3. Due to symmetry, only half of the thickness of the disc is modelled.

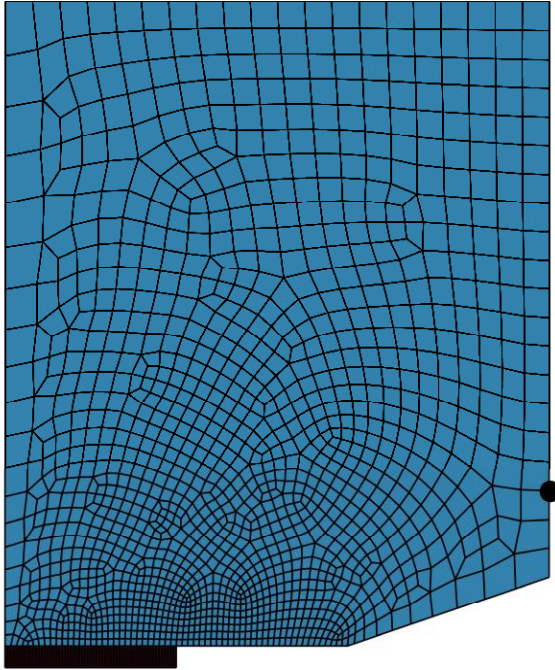


Figure 3. Two-dimensional axisymmetric model showing Bridgman anvil and 5 mm specimen. The black dot is representing the measured displacement location

The tooling was modelled as elastic using a material model corresponding to tungsten carbide containing 6 wt% Cobalt. The powder compacts were modelled using 600 elements. The dimensions and densities of the compacts were as follows:

- Thickness=5.0 mm, diameter=40.0 mm and initial density=1811 kg/m<sup>3</sup>.

To model the concentric rings, that are press fitted on to the anvil as support, a 200 MPa pressure was applied to the outer diameter of the anvil. The numerical calculations were done according to the time schedule presented in Table 1. The numerical model used for the high friction set-up was the same as mentioned above. To reduce calculation time a mass scaling was introduced by increasing the density 1000 time.

Table 1. Time schedule

Process	Start	End
Anvil support	0.0 sec	0.1 sec
Loading	0.1 sec	0.5 sec
Unloading	0.5 sec	0.8 sec

In Berg et al. (2012c) an instrumented Bridgman anvil press was used to record the mean stress. The stress in the disc is measured using a bismuth (Bi) wire mounted at different positions in the disc. Bismuth has three phase transitions occurring at the isostatic pressures of 2.55, 2.70 and 7.70 GPa, where 2.55 and 7.70 are commonly used. The average load at each phase transition was reported. However, the phase transitions had different start and end values. From the results the absolute value of the mean stress at the different positions was found corresponding to the phase transition pressures. The numerical results are compared to the experimental results. The load versus thickness is shown in Figure 4. In Table 2 the calculated and measured forces at phase transitions are shown. Finally, the calculated mean stress distribution is plotted against the initial radius and compared to experimental phase transition points.

As shown in Figure 4 the up-ramp phase is in good agreement between the experimental and the numerical results. However, the calculated down-ramp (unloading) shows some divergence from the experimental measurements. The compression in the numerical analysis is 2.55 mm compared to the measured 2.75 mm which gives an error of approximate 7%.

In Table 2 the experimental and numerical results can be seen together with the error. The values that are compared are the average load at the phase transition. The first phase transition during the up-ramp occurs at 2.55 GPa (centre of the disc). The error was calculated to -8%, for the 7.7 GPa phase transition the error was 8%. For a radius of 10 mm, the error was -5%. In general, the uncertainty of the measured phase transitions are  $\pm 0.06$  GPa at 2.55 GPa and  $\pm 0.2$  GPa at 7.7 GPa (Bean et al, 1986; Peggs, 1983) this is during isostatic conditions. The uncertainty of measurements under non-isostatic condition is probably higher. Also, comparison of the down-ramp values can be seen in Table 2. At the 2.55 GPa phase transition, in the centre of the disc, the error was 25%. From the numerical model phase transitions occur at a lower load than the experiments. In total load difference, it is only about 100 kN. From the load-thickness curves. For the 7.7 GPa phase transition the error was 37%. At the radius of 10 mm, the error was 12%. The down-ramp phase transitions comparison is probably affected by the fact that in the experiment the disc is cracking.

The calculated pressure profile has been plotted versus the initial radius and is compared to experimental phase transition points. The pressure profiles were plotted for three different loads, 991 kN, 2991 kN and maximum load. Further, 5% uncertainty was added to the load value of the experimental pressure points, see Figure 5. The 5% seem to be inline with the error found in Berg et al. (2012c). The maximum pressure reaches about 9 GPa. Comparing the pressure profile at around 3000 kN load to the experimental pressure points ( $r=0$  and  $r=10$  mm) it can be seen that the calculated pressure is close to the experimental measured pressure. At the lowest load, around 1000 kN, the pressure profile is flatter than at higher loads. Overall the main features of the virtually reproduced pressure distribution compares well to the experimentally measured pressure.

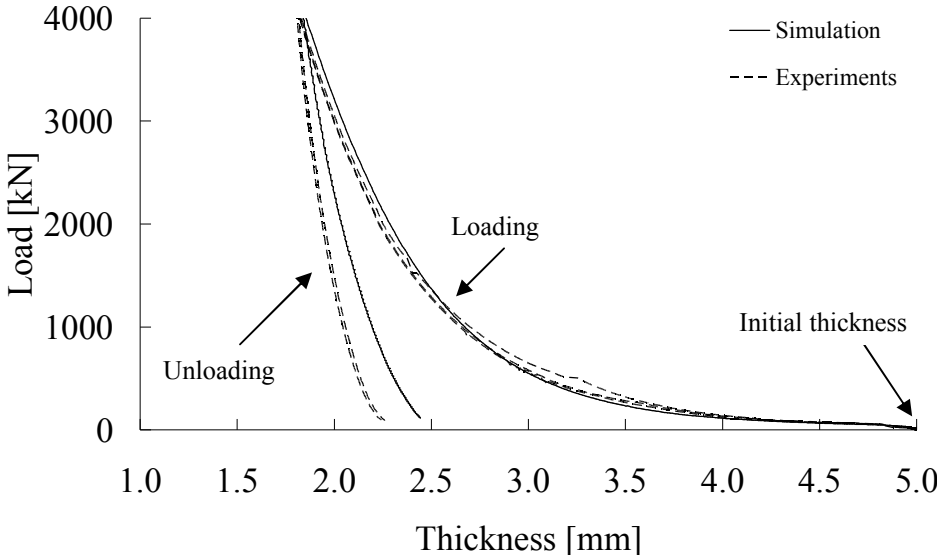


Figure 4. Load - thickness curve comparison between experiment (Berg et al., 2012b) and analysis

Table 2. Comparison of experiment and analysis for up and down-ramp load at Bi phase transitions

Phase transition [GPa]	Ramp	Radius [mm]	Load Exp. [kN]	Load Sim. [kN]	Error [%]
2.55	Up	0	997	918	-8
7.70	Up	0	2978	3221	8
2.55	Up	9.7	3139	2991	-5
2.55	Down	0	274	206	-25
7.70	Down	0	1810	2480	37
2.55	Down	9.7	2774	3107	12

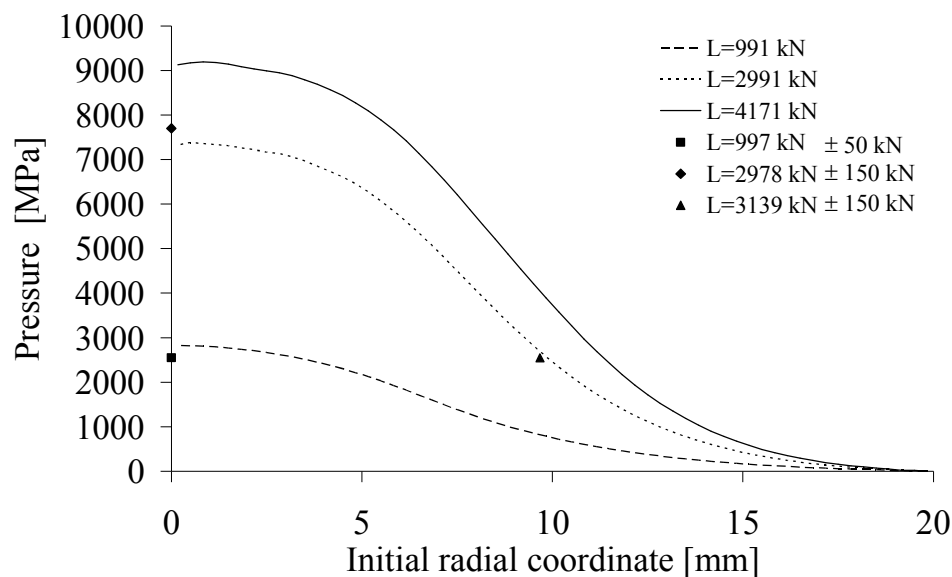


Figure 5. Comparison of analysis and measurement. Calculated mean stress (pressure) versus radial coordinate in the powder disc for three different load levels. Two load levels are chosen as close as possible, from the numerical output, as the load level of measured Bi phase transitions. Measured stresses are marked with symbols. The third stress profile is at maximum load (4171 N), no experimental results for this load.

One possible reason for the deviation in the results between experiment and analysis, in term of pressure and load, is that the friction coefficient may possible varies over the anvil face depending on pressure. Further, the friction may be lower at start-up as shown by Berg et al. (2012c). In addition, the phase transition of the  $\text{CaCO}_3$  has not taken into account in the analysis. There are three transitions occurring, two at about 1.5-1.8 and one at 2.3-3.5 GPa, see Fiquet et al. (1994). The latter one is the larger of the two and covers the Bi phase transition at 2.55 GPa. Depending on the large pressure gradient, the transitions probably occur gradually through the disc and are then not seen as a jump in the thickness curve.

## 5 Conclusion

A constitutive model for high-pressure compaction has been developed. The model is able to virtually reproduce the mechanical process of pressing powder from low density to full density. The ability to account for ultra high stress states is another unique feature of the model. The constitutive model was implemented as a user subroutine in a finite element code. Numerical analysis of compacting  $\text{CaCO}_3$  powder disc in a Bridgman anvil apparatus was reproduced. The numerical model was validated against the experimental results comparing the loads at the phase transition of Bi-wires. Compressive mean stresses of more than 9 GPa were reached inside the powder compact according to the calculation. In conclusion, the results obtained by the numerical analysis agree well with the experimental measurements during the compaction phase. During the unloading phase the measured stress in the centre of the sample does not agree well with the calculations. The main reason for this is the cracking of the sample.

## References

- Akaishi, M.; Yamaoka, S.; Ueda, F.; Ohashi, T.: Synthesis of polycrystalline diamond compact with magnesium carbonate and its physical properties, *Diamond and Related Materials*, 5, (1996), 2-7.
- Bean V.E.; Akimoto, S.; Bell, P.M.; Block, S.; Holzapfel, W.B.; Manghnani, M.H.; Nicol, M.F.; Stiahov, S.M.: Physica, Another Step Toward an International Practical Pressure Scale 2nd AIRAPT IPPS Task Group Report (1986), 139 & 140B, 52-54.
- Berg, S.; Jonsén, P.; Häggblad, H.-Å.: Experimental characterisation of CaCO<sub>3</sub> powder mix for high pressure compaction modelling, *Powder Technology*, 203, (2010), 198-205.
- Berg, S.; Häggblad H.-Å.; Jonsén, P.: High Pressure Compaction Modelling of Calcite (CaCO<sub>3</sub>) powder compact, *Powder Technology*, 206, (2011), 259-268.
- Berg, S.; Marklund, P.; Häggblad, H.-Å.; Jonsén P.: Frictional behaviour of CaCO<sub>3</sub> powder compacts, (2012a) (To be published).
- Berg, S.; Jonsén, P.; Häggblad, H.-Å.; Carlson, J.: Ultra high-pressure characterization and modelling of CaCO<sub>3</sub> powder mix in the Bridgman anvil apparatus, (2012b) (To be Published).
- Berg, S.; Häggblad, H.-Å.; Jonsén, P.: Experimental characterization of CaCO<sub>3</sub> powder for use in compressible gaskets up to ultra-high pressure, *Powder Technology*, 215-216, (2012c), 124-131 .
- Brinckmann, S.; Gao, G.; Siegmund, T.: A combined experimental–numerical study of the compaction behavior of NaCl, *Powder Technology*, 194, (2009), 197-206.
- Carlson, J.; Nilsson, M.; Fernández, E.; Planell, J.A.: An ultrasonic pulse-echo technique for monitoring the setting of CaSO<sub>4</sub>-based bone cement, *Biomaterials*, 24, (2003), 71-77.
- Fiquet, G. Guyor, F. Itié, J.-P.: High-pressure X-ray diffraction study of carbonates: MgCO<sub>3</sub>, CaMg(CO<sub>3</sub>)<sub>2</sub>, and CaCO<sub>3</sub>, *American Mineralogist*, 79, (1994), 15-23.
- Fukuhara, M.; Wada, T.; Inoue, A.: Ultrasonic characteristics of porous Pd<sub>42.5</sub>Cu<sub>30</sub>Ni<sub>7.5</sub>P<sub>20</sub> glassy alloy, *Journal of applied physics*, 102, (2007).
- Fukunaga, O.; Ko Y.S.; Konoue, M.; Ohashi, N.; Tsurumi, T.: Pressure and temperature control in flat-belt type high pressure apparatus for reproducible diamond synthesis, *Diamond and Related Materials*, 8, (1999), 2036-2042.
- Gallas, M.R.; Rosa, A.R.; Costa, T.H.; da Jornada, J.A.H.: High pressure compaction of nanosize ceramic powders, *J. Mater. Res.*, 12, (3), (1997), 764-768.
- Grady, D.E.: Compression Wave Studies on Calcite Rock, *Shock Journal of Geophysical Research*, Volume. 83, No. B6, (1978), 2839-2849.
- Graham, E.K.: Recent Developments in Conventional High-Pressure Methods, *Journal of Geophysical Research.*, 91 (B5), (1986), 4630-4642.
- Han, L.H.; Elliott J.A.; Bentham, A.C.; Mills, A.; Amidon, G.E.; Hancock, B.C.: A modified Drucker-Prager Cap model for die compaction simulation of pharmaceutical powders, *International Journal of Solids and Structures*, 45, (2008), 3088-3106.
- Häggblad, H.-Å.: Constitutive models for powder materials, *Powder Technology.*, 67 (2), (1991), 127-136.
- Jonsén, P.; Häggblad, H.-Å.: Modelling and numerical investigation of the residual stress state in a green metal powder body, *Powder Technology*, 155, (3), (2005), 196-208.

- Kanke, Y.; Akaishi, M.; Yamaoka, S.; Taniguchi, T.: Heater cell for materials synthesis and crystal growth in the large volume high pressure apparatus at 10 GPa, *The Review of Scientific Instruments*, 73 (9), (2002), 3268–3270.
- Knittle, E.: Static pressure measurements of equation of state, *Mineral physics & crystallography: a handbook of physical constants, Vol. 2, American Geophysical Union, Washington, D.C.*, (1995), 98-142.
- Li, Y.-L.; Liang, Y.; Zheng, F.: Sintering of nanopowders of amorphous silicon nitride under ultrahigh pressure, *J. Mater. Res.*, 15(4), (2000), 988-994.
- Li, R.; Ma, H.A.; Han, O.G.; Liang, Z.Z.; Yin, B.H.; Liu, W.O.; Jia, X.: Simulation of pressure distribution in a Pyrophyllite high-pressure cell by finite-element analysis, *High Pressure Research*, 27 (2), (2007), 249-257.
- Lu, T.C.; Chang, H.; Qi, J.Q.; Luo, X.J.: Low temperature high-pressure preparation of transparent nanocrystalline MgAl<sub>2</sub>O<sub>4</sub> ceramics, *Applied Physics letter*, 88, (2006), 213120.
- Peggs G.N. (ed.): High Pressure Measurement Techniques, 1983 (Applied Science Publishers, London UK)
- Sandler, I.S.; Baron, M.L.: Recent developments in constitutive modelling of geological materials, *Third International Conference on numerical methods in Geomechanics*, Aachen, 2-6 April, (1979), 363-376.
- Sandler, I.S.; DiMaggio, F.L.; Asce, F.; Baladi, G.Y.; Asce, M.: Generalized Cap Model For Geological Materials, *Journal of the Geotechnical Engineering Division*., (1976), 683-699.
- Sandler, I.S.; Rubin, D.: An algorithm and a modular subroutine for the cap model, *International Journal for Numerical and Analytical Methods in Geomechanics*., 3 (1979), 173-186.
- Sumiya, H.; Satoh S.: Synthesis of polycrystalline diamond with new non-metallic catalyst under high pressure and high temperature, *International Journal of Refractory Metals & Hard Materials*, 17, (1999), 345-350.
- Sung, C-M.: A Century of progress in the development of very high pressure apparatus for scientific research and diamond synthesis, *High Temperatures – High Pressures*, 29, (1997), 253-293.
- Taniguchi, T.; Akaishi, M.; Kanke Y.; Yamaoka, S.: TiC-diamond composite discheater cell assembly to generate temperature of 2000°C in a large-volume belt type high-pressure apparatus at 10 GPa, *The Review of Scientific Instruments*, 75 (6), (2004), 1959–1962.
- Svoboda, A.; Häggblad, H-Å.; Näsström, M.: Simulation of hot isostatic pressing of metal powder components to near net shape. *Engineering Computations*, 13, (2006), 13-37.
- Ueda, F.; Ohashi, T.; Akaishi, M.; Yamaoka, S.: Cutting performance of sintered diamond with MgCO<sub>3</sub> as a sintering agent, *Materials Science and Engineering*, A209, (1996), 260-263.
- Wakatsuki, M.; Ichinose, K.; Aoki, T.: Notes on Compressible Gasket and Bridgman-Anvil Type High Pressure Apparatus, *Japanese Journal of Applied Physics*. 11 (4), (1972), 578-590.
- Westraadt, J.E.; Dubrovinskaia, N.; Neethling J.H.; Sigalas, I.: Thermally stable polycrystalline diamond sintered with calcium carbonate, *Diamond & Related Materials*, 16, (2007), 1929–1935.

## Appendix A: Explicit Time Integration in FEM

A transfer of a continuous system to a system with limited number of degrees of freedom (dof) is the idea behind the finite element method. For dynamic problems in structural dynamics are frequently solved by application of explicit time integration methods. These methods can be implemented easily and they require only low amount of storage capacity. A drawback is the stability of the methods as there is a critical time step, which must not be exceeded.

### Notation

Displacements	$\{u\} = \begin{bmatrix} u_x(x, y, z, t) \\ u_y(x, y, z, t) \\ u_z(x, y, z, t) \end{bmatrix}$	Surface load	$\{\Phi\} = \begin{bmatrix} \Phi_x \\ \Phi_y \\ \Phi_z \end{bmatrix}$
Volume loads	$\{F\} = \begin{bmatrix} F_x \\ F_y \\ F_z \end{bmatrix}$	Point loads	$\{P\}_i = \begin{bmatrix} P_x \\ P_y \\ P_z \end{bmatrix}_i$
Strains	$\{\varepsilon\} = \begin{bmatrix} \varepsilon_{xx} \\ \varepsilon_{yy} \\ \varepsilon_{zz} \\ \gamma_{xy} \\ \gamma_{yz} \\ \gamma_{zx} \end{bmatrix}$	Stresses	$\{\sigma\} = \begin{bmatrix} \sigma_{xx} \\ \sigma_{yy} \\ \sigma_{zz} \\ \sigma_{xy} \\ \sigma_{yz} \\ \sigma_{zx} \end{bmatrix}$
Nodal displacements	$\{d\} = \begin{bmatrix} d_{1x} \\ d_{1y} \\ d_{1z} \\ d_{2x} \\ d_{2y} \\ \cdot \\ \cdot \end{bmatrix}$		

---

Applying the principle of virtual work on a volume for a small change in displacement  $\{\delta u\}$  and corresponding change in strain  $\{\delta \varepsilon\}$  outer work and inner energy have to be equal

$$\begin{aligned}
 & \int_{V_e} \{\delta u\}^T \{F\} dV + \int_{S_e} \{\delta u\}^T \{\Phi\} dS + \sum_{i=1}^n \{\delta u\}_i^T \{P\}_i \quad (\text{outer work}) \\
 & = \int_{V_e} \left( \{\delta \varepsilon\}^T \{\sigma\} + \{\delta u\}^T \rho \{\ddot{u}\} + \{\delta u\}^T \kappa_d \{\dot{u}\} \right) dV \quad (\text{inner energy})
 \end{aligned} \tag{A.1}$$

In applying the FEM assumption we separate space and time dependent variables. The displacements  $u$  at any position in space of the element may be found by shape functions  $N$  also called interpolation functions. The nodal displacement  $d$  is time dependent variable

$$\{u\} = [N] \{d\} \tag{A.2}$$

Velocity  $\dot{u}$ , acceleration  $\ddot{u}$  and change in strain  $\delta \varepsilon$  inside the element can also be found

$$\{\dot{u}\} = [N]\{\dot{d}\} \quad (\text{A.3})$$

$$\{\ddot{u}\} = [N]\{\ddot{d}\} \quad (\text{A.4})$$

$$\{\delta\varepsilon\} = [B]\{\delta d\} \quad (\text{A.5})$$

where  $B$  is the strain-displacement matrix. Applying the FEM assumption to the energy equilibrium equation (A.1) above gives

$$\begin{aligned} \{\delta d\}^T \left[ \int_{V_e} [B]^T \{\sigma\} dV + \int_{V_e} \rho [N]^T [N] dV \{\ddot{d}\} + \int_{V_e} \kappa_d [N]^T [N] dV \{\dot{d}\} \right. \\ \left. - \int_{V_e} [N]^T \{F\} dV - \int_{S_e} [N]^T \{\Phi\} dS - \sum_{i=1}^n \{P\}_i \right] = 0 \end{aligned} \quad (\text{A.6})$$

The expression within  $[ ] = 0$  as the whole expression should be  $= 0$  for any  $\{\delta d\}$ .

In explicit non-linear FEM the equation of motion is solved

$$[m]\{\ddot{d}\} + [c]\{\dot{d}\} + \{r^{\text{int}}\} = \{r^{\text{ext}}\} \quad (\text{A.7})$$

where the element mass matrix  $[m]$  is defined as

$$[m] = \int_{V_e} \rho [N]^T [N] dV \quad (\text{A.8})$$

and the damping  $[c]$  matrix is

$$[c] = \int_{V_e} \kappa_d [N]^T [N] dV \quad (\text{A.9})$$

In FEM the inner load is defined as

$$\{r^{\text{int}}\} = \int_{V_e} [B]^T [\sigma] dV \quad (\text{A.10})$$

and outer load is

$$\{r^{\text{ext}}\} = \int_{V_e} [N]^T \{F\} dV + \int_{S_e} [N]^T \{\Phi\} dS + \sum_{i=1}^n \{P\}_i \quad (\text{A.11})$$

Assuming linear elastic material Hook's law is used

$$\{\sigma\} = [E]\{\varepsilon\} = [E][B]\{d\} \quad (\text{A.12})$$

now the inner load can be rewritten

$$\{r^{\text{int}}\} = \underbrace{\int_{V_e} [B]^T [E][B] dV}_{[k]} \{d\} = [k]\{d\} \quad (\text{A.13})$$

This gives

$$[m]\{\ddot{d}\} + [c]\{\dot{d}\} + [k]\{d\} = \{r^{ext}\} \quad (\text{A.14})$$

for the assembled system of elements the expression is usually written

$$[M]\{\ddot{D}\} + [C]\{\dot{D}\} + [K]\{D\} = \{R^{ext}\} \quad (\text{A.15})$$

Direct integration start from the equation of motions derived with the FE-method and then the integration is applied. Equations of motions in matrix form at the time,  $t=n*\Delta t$ , becomes

$$[M]\{\ddot{D}\}_n + [C]\{\dot{D}\}_n + [K]\{D\}_n = \{R^{ext}\}_n \quad (\text{A.16})$$

The equation is in dynamic equilibrium at time step  $n$ ,  $t = t_n$ . If the equilibrium is applied to the equation of motion without damping

$$[M]\{\ddot{D}\}_n + [K]\{D\}_n = \{R^{ext}\}_n \quad (\text{A.17})$$

and differentiated with the central difference method using

$$\dot{d}_n = \frac{1}{2\Delta t}(d_{n+1} - d_{n-1}). \quad (\text{A.18})$$

The second derivative derived from the central difference method

$$\begin{aligned} \ddot{d}_n &= \frac{1}{\Delta t} \left( \dot{d}_{n+\frac{1}{2}} - \dot{d}_{n-\frac{1}{2}} \right) = \frac{1}{\Delta t} \left( \frac{1}{\Delta t}(d_{n+1} - d_n) - \frac{1}{\Delta t}(d_n - d_{n-1}) \right) \\ &= \frac{1}{\Delta t^2} (d_{n+1} - d_n - d_n + d_{n-1}) = \frac{1}{\Delta t^2} (d_{n+1} - 2d_n + d_{n-1}) \end{aligned} \quad (\text{A.19})$$

The second derivative is calculated in the middle of the time step.

If the central difference method is taken for the whole system with first and second derivative

$$\{\dot{D}\}_n = \frac{1}{2\Delta t} (\{D\}_{n+1} - \{D\}_{n-1}) \quad (\text{A.20})$$

$$\{\ddot{D}\}_n = \frac{1}{\Delta t^2} (\{D\}_{n+1} - 2\{D\}_n + \{D\}_{n-1}) \quad (\text{A.21})$$

and put into equation (A.17) gives

$$[M] \left( \frac{1}{\Delta t^2} (\{D\}_{n+1} - 2\{D\}_n + \{D\}_{n-1}) \right) + [K]\{D\}_n = \{R^{ext}\}. \quad (\text{A.22})$$

Equation (A.22) can be rewritten as

$$\frac{1}{\Delta t^2} [M]\{D\}_{n+1} = \{R^{ext}\}_n - [K]\{D\}_n + \frac{1}{\Delta t^2} [M](2\{D\}_n - \{D\}_{n-1}) \quad (\text{A.23})$$

and the solution for the system is

$$\{D\}_{n+1} = 2\{D\}_n - \{D\}_{n-1} + \Delta t^2 [M]^{-1} (\{R^{ext}\}_n - \{R^{int}\}_n) \quad (\text{A.24})$$

where

$$\{R^{int}\}_n = [K]\{D\}_n = \sum_{elem V_e} \int [B]^T \{\sigma\}_n dV \quad (A.25)$$

The solutions in equation (A.24) are uncoupled equations if [M] is a lumped mass matrix (diagonal matrix) and that implies that no equation system needs to be solved. In a FE-calculation the velocities are usually stored between time steps, this gives another formulation. In equation (A.19) the second derivative can be reformulated as

$$\ddot{d}_n = \frac{1}{\Delta t} \left( \dot{d}_{n+\frac{1}{2}} - \dot{d}_{n-\frac{1}{2}} \right) \Rightarrow \dot{d}_{n+\frac{1}{2}} = \dot{d}_{n-\frac{1}{2}} + \Delta t \ddot{d}_n \quad (A.26)$$

Exploiting the first derivative equation (A.18) for half the time step

$$\dot{d}_{n+\frac{1}{2}} = \frac{1}{\Delta t} (d_{n+1} - d_n) \quad (A.27)$$

and put equation (A.26) into equation (A.27) gives

$$\frac{1}{\Delta t} (d_{n+1} - d_n) = \dot{d}_{n-\frac{1}{2}} + \Delta t \ddot{d}_n \Rightarrow d_{n+1} = d_n + \Delta t \dot{d}_{n-\frac{1}{2}} + \Delta t^2 \ddot{d}_n \quad (A.28)$$

For the system the solution can be written as

$$\{D\}_{n+1} = \{D\}_n + \Delta t \{\dot{D}\}_{n-\frac{1}{2}} + \Delta t^2 \{\ddot{D}\}_n \quad (A.29)$$

but known from equation of motion equation (A.17)

$$[M]\{\ddot{D}\}_n = \{R^{ext}\}_n - \{R^{int}\}_n \Rightarrow \{\ddot{D}\}_n = [M]^{-1} \left( \{R^{ext}\}_n - \{R^{int}\}_n \right) \quad (A.30)$$

Put equation (A.30) into equation (A.29) the solution of the system will be

$$\{D\}_{n+1} = \{D\}_n + \Delta t \{\dot{D}\}_{n-\frac{1}{2}} + \Delta t^2 [M]^{-1} \left( \{R^{ext}\}_n - \{R^{int}\}_n \right) \quad (A.31)$$

and updating the velocities for the next step

$$\{\dot{D}\}_{n+\frac{1}{2}} = \{\dot{D}\}_{n-\frac{1}{2}} + \Delta t \{\ddot{D}\}_n \quad (A.32)$$

For the central difference method a starting conditions is needed. At  $t = 0$  the solution has to be rewritten as

$$\{D\}_1 = \{D\}_0 + \Delta t \{\dot{D}\}_0 + \frac{1}{2} \Delta t^2 [M]^{-1} \left( \{R^{ext}\}_0 - \{R^{int}\}_0 \right) \quad (A.33)$$

and updating the velocities for the next step is given as

$$\{\dot{D}\}_{\frac{1}{2}} = \{\dot{D}\}_0 + \frac{1}{2} \Delta t \{\ddot{D}\}_0 \quad (A.34)$$

## Appendix B: Stability Condition

Explicit time integration is effective and usual method in numerical calculation. The method is a conditionally stable method meaning that the time step should not exceed the critical time step. For explicit integration the stability condition is

$$\Delta t \leq \frac{2}{\omega_{\max}} \quad (\text{B.1})$$

where  $\omega_{\max}$  is the highest eigenfrequency of the structure

$$\omega_{\max} \approx \frac{2c}{L_e} \quad (\text{B.2})$$

where  $c$  is wave propagation velocity and  $L_e$  is a characteristic length in the structure (smallest distance between two nodes). The Courant's stability condition

$$\Delta t \leq \frac{L_e}{c} \quad \text{where} \quad c = \sqrt{\frac{E}{\rho}} \quad (\text{B.3})$$

where  $E$  is Young's modulus and  $\rho$  is the density. The time step must be shorter than the time needed for a 1-D wave to propagate the length  $L_e$ . The smallest element side will limit the time step in the explicit numerical analysis.

---

*Address:* Assoc. Prof. Dr.-Ing. Pär Jonsén and Prof. Dr.-Ing. Hans-Åke Häggblad, Division of Mechanics of Solid Materials, Luleå University of Technology, SE-971 87 Luleå.  
email: par.jonsen@ltu.se; hans-åke.haggblad@ltu.se .